ABSTRACT

SUVARNA, SUSHIL SHEENA. Reconstruction of Ground Penetrating Radar Images Using Techniques based on Optimization. (Under the guidance of Dr Wesley Snyder and Dr Leonhard Bernold)

Ground Penetrating Radar (GPR) is an instrument used in semi-automated construction systems. In principal, images of subsurface objects such as pipes and mines may be detected and potentially measured. The detection of utilities is complicated by a combination of the complexity involved in the data collection technique of the GPR and the irregularities present beneath the surface. This thesis provides the initial results in the development of an algorithm to invert the effects of these corruptions and return images, which are exact in the placement and conformation of subterranean objects. The technique employed is a deconvolution-like method that utilizes a maximum a posteriori (MAP) based optimization method to estimate the best reconstruction. Mean field annealing (MFA) using gradient descent is the optimization method used. Using this technique, single objects in the field of observation were reconstructed to within an acceptable percentage of their original shape. Further work would involve reconstructing multiple objects in the field of observation as well as considering features other than hyperbolae that correspond to objects.

RECONSTRUCTION OF GROUND PENETRATING RADAR IMAGES USING TECHNIQUES BASED ON OPTIMIZATION

by

SUSHIL SHEENA SUVARNA

A thesis submitted to the Graduate Faculty of
North Carolina State University
in partial fulfillment of the
requirements for the Degree of
Master of Science

COMPUTER SCIENCE

Raleigh

2004

APPROVED BY:

_____	_____
Dr Douglas Reeves	Dr Mladen Vouk
_____	_____
Dr Wesley Snyder Chair of Advisory Committee	Dr Leonhard Bernold Co-Chair of Advisory Committee

BIOGRAPHY

Sushil S. Suvarna was born on December 24, 1979 in the city of Bombay, India. He completed his Bachelors Degree in Electronics Engineering from Padmabhushan Vasantdada Patil Pratishthan College of Engineering, Bombay, in May 2001. He then joined North Carolina State University in Aug 2001, to further a Masters Degree in Computer Science. During his time at NCSU, he worked on research projects along with Dr L. Bernold and Dr W. Snyder.

TABLE OF CONTENTS

LIST OF FIGURES ..... **iv**

1. PROBLEM DESCRIPTION **1**
1.1 INTRODUCTION 1
1.2 WHAT IS A GPR? 1
1.3 MATERIAL CONDUCTIVITY 2
1.4 DATA MIGRATION 4
1.4.1 Data misrepresentation caused by the transmitted signal (direct wave) *4*
1.4.2 Data misrepresentation caused by the signal spread *6*

2. LITERATURE REVIEW **9**
2.1 GPR ANTENNA CHARACTERIZATION 9
2.2 CATEGORIZATION OF OBJECT RECONSTRUCTION TECHNIQUES 12
2.3 GPRS USED IN MINE DETECTION 14
2.4 RECONSTRUCTIONS BASED ON OPTIMIZATION 15
2.5 ALGORITHMS FOR THE INVERSION OF THE TRANSMITTED WAVE 16
2.6 MIGRATION ALGORITHMS 18

3. OPTIMIZATION ALGORITHM **21**
3.1 CONSTRUCTING THE OBJECTIVE FUNCTION 21
3.2 GRADIENT DESCENT 24
3.3 MEAN FIELD ANNEALING 26

4. PRIMARY PROCESSING OF THE RECEIVED GPR SIGNAL **28**
4.1 BACKGROUND REMOVAL USING "SUBTRACT TRANSMITTED PULSE" 29
4.2 BACKGROUND REMOVAL USING "SUBTRACT MEAN TRACE" 30

5. DATA MIGRATION **33**
5.1 CORRELATION OF THE TRANSMITTED SIGNAL 33
5.1.1 Signal Description and Simulation *33*
5.1.2 Linear Correlation Coefficient (LCC) *35*
5.2 ANTENNA SIGNAL SPREAD 41
5.2.1 Incorporating the Prior and Noise Terms *41*
5.2.2 Gradient Descent and the MFA Algorithm *46*

6. CONCLUSION **52**

7. FUTURE WORK **54**

BIBLIOGRAPHY **56**

LIST OF FIGURES

FIGURE 1-1 SAMPLE IMAGE OF THE GPR....07

FIGURE 1-2 ADDIITION OF THE TRANSMITTED SIGNAL OF THE GPR....09

FIGURE 1-3. SAMPLE TRANSMITTED WAVE OF THE GPR.....10

FIGURE 1-4. SIGNAL SPREAD OF THE GPR REPRESENTED AS A CONE....11

FIGURE 1-5. EFFECTS OF THE SIGNAL SPREAD....13

FIGURE 1-4. HYPERBOLIC REPRESENTATIONS OF OBJECTS....13

FIGURE 2-1. ELECTRIC AND MAGNETIC PATTERNS FOR A GPR ANTENNA (FROM [26])....16

FIGURE 2-2. "THE RICKER WAVELET" (FROM [34])....21

FIGURE 2-3. "THE GPR WAVELET" (FROM [34])....21

FIGURE 2-4. COHERENT SUMMATION (FROM [18])....24

FIGURE 3-1. FLOW DIAGRAM OF THE SYSTEM....27

FIGURE 4-1. RAW DATA FROM THE GPR....33

FIGURE 4-2-1. INITIAL UNFILTERED GPR DATA....35

FIGURE 4-2-2. FILTERED DATA (SUBTRACT TRANSMITTED PULSE)....35

FIGURE 4-3-1. INITIAL UNFILTERED GPR DATA....36

FIGURE 4-3-2. FILTERED DATA (SUBTRACT MEAN TRACE)....36

FIGURE 4-4-1. SUBTRACT MEAN TRACE – WINDOW SIZE 30....36

FIGURE 4-4-2. SUBTRACT MEAN TRACE – WINDOW SIZE 200....36

FIGURE 5.1. GAUSSIAN MODULATED SINE WAVE MODEL OF THE GPR SIGNAL....39

FIGURE 5.2. SIMULATED DISK PLACED UNDER THE SOIL SURFACE....40

FIGURE 5.3. RECEIVED GPR IMAGE (SIMULATED)....41

FIGURE 5.4. COLUMN (1-D) REPRESENTATION OF THE DISK....43

FIGURE 5.5. RESULT OF THE CORRELATION (1-D)....44

FIGURE 5.6. RECONSTRUCTED IMAGE (1-D)....45

FIGURE 5.7. FILTERED GPR IMAGE 46
FIGURE 5.8. RESULT OF THE LCC TECHNIQUE ON REAL DATA 46
FIGURE 5.9. SIGNAL SPREAD OF THE GPR 48
FIGURE 5.10. SIMULATED DISK PLACED BENEATH THE SURFACE 54
FIGURE 5.11. HYPERBOLIC REPRESENTATION OF TE DISK (SIMULATED) 54
FIGURE 5.12. RECONSTRUCTION OF THE DISK USING MFA 55
FIGURE 5.13. WHAT THE COMPLETE DISK WOULD LOOK LIKE 55
FIGURE 5.14. ENERGY CURVE OF THE MFA ALGORITHM 56
FIGURE 5.15. GRAPH OF SIGNAL TO NOISE RATIO VS ERROR 57
FIGURE 7.1. TWO DISKS PLACED SIDE BY SIDE (SIMULATED) 60
FIGURE 7.2. HYPERBOLIC REPRESENTATION OF THE TWO DISKS (SIMULATED) 60
FIGURE 7.3. ATTEMPTED RECONSTRUCTION OF THE TWO DISKS (SIMULATED) 61

1. PROBLEM DESCRIPTION

1.1 INTRODUCTION

Ground Penetrating Radar (GPR) is an instrument that is used for subsurface mapping using high-frequency electromagnetic waves. We attempt to use this instrument to detect, locate and measure buried utilities, primarily pipes, both metallic and non-metallic. The first part of the thesis explains the complex transmitted wave, constructs a model that best represents this wave, and presents a method based on correlation and thresholding that locates the pipes. The second half focuses on the signal-spread of the transmitted wave of the GPR, which appears more as a cone than a single vertical pulse. This spread causes migration of the object, and we propose a method based on optimization to invert this distortion. Finally, a common algorithm comprised of the above methods is applied to actual GPR data in real time to extract all the possible object locations with minimum false positives.

1.2 WHAT IS A GPR?

GPR transmits short pulses of high frequency electromagnetic energy into the ground from a transmitting antenna. These waves propagate into the ground with a velocity that depends on the dielectric property of the medium. If the waves encounter an interface between two materials with different refractive indices, some of the wave energy is reflected back and the rest continues to propagate to create further reflections. A receiver picks up these reflections and processes them to create an image as shown in Fig 1.1.

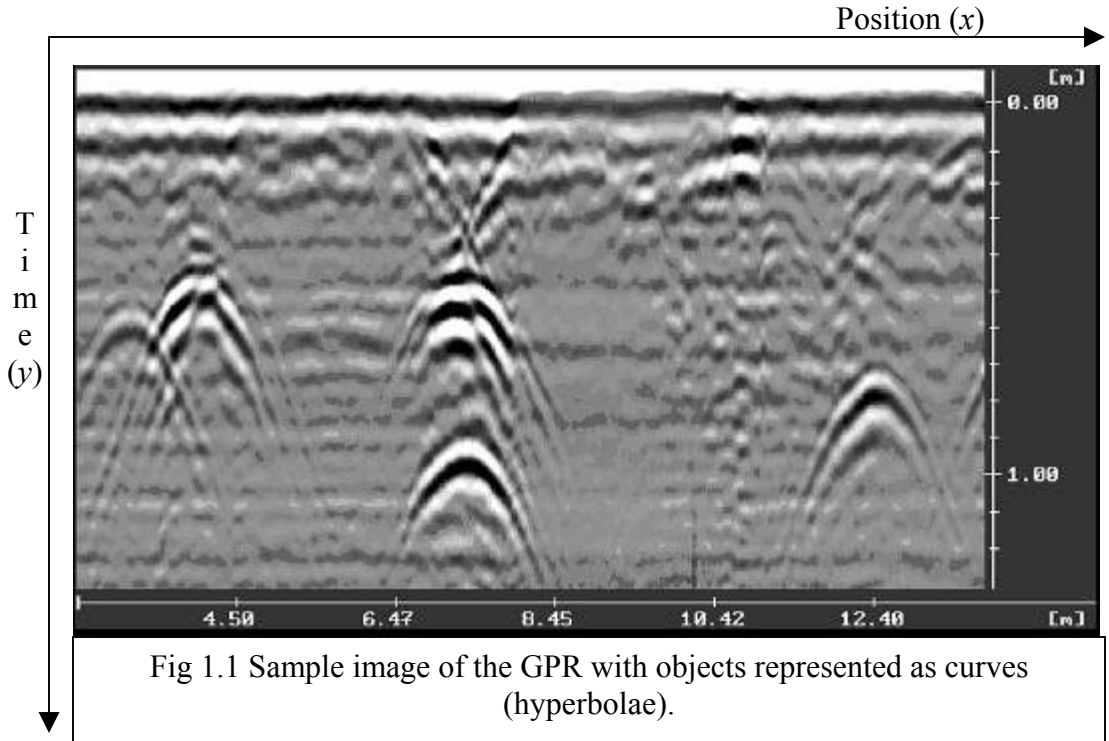

Fig 1.1 Sample image of the GPR with objects represented as curves (hyperbolae).

In order to create an image, the GPR sends out pulses at a certain frequency and samples the responses for a certain time slot before recording them as a single column corresponding to a single position of the GPR. A collection of these columns, representing different positions recorded in continuance make up an image.

1.3 MATERIAL CONDUCTIVITY

The type of material in which the waves of the GPR propagate has a strong effect on the signal penetration and the clarity of the received wave. The different material interfaces that the wave encounters affect its amplitude and phase. The received data consists of a) changes

in reflection strength, b) changes in arrival time of specific reflections, c) source wavelet distortion, and d) signal attenuation.

The GPR data consists of a continuous graphic display of reflected energy over a set time interval. This set time interval is the two-way travel time, measured in nanoseconds. The depth of the material the wave penetrates can be determined if the velocity of the electromagnetic energy (v_m) through the material is known. Using the dielectric constant of the material, the velocity of the wave can be calculated using the formula

$$v_m = \frac{c}{\sqrt{\varepsilon_r}},$$

where c is the speed of light in vacuum and ε_r is the dielectric constant of the medium.
Once the speed is known, the depth of a particular object in the image can be calculated by using the formula

$$d_r = \frac{v_m t_r}{2}.$$

d_r is the depth, v_m is the velocity in the medium and t_r is the two way travel time from the GPR to the object.

The penetration depths achieved using the GPR depend on the signal frequency and on the nature of the material in which it travels. Higher frequency electromagnetic waves give better resolution, but cannot penetrate to a great depth. Lower frequencies on the other hand penetrate much deeper but provide poorer resolution. The wave will easily penetrate resistive materials and will not heavily penetrate conductive materials. Because of their higher conductivity, dense, moist clays impede the performance of the GPR, and saltwater makes

the technique ineffective. Electromagnetic energy, in these frequency ranges, seldom penetrates more that 30m into the surface and, in highly conductive material, may only penetrate a few meters.

1.4 DATA MIGRATION

Migration is a technique that is used to relocate objects in a GPR image from where they appear to be, to where they are actually located.

GPR data is misrepresented in two ways, a) due to the structure of the transmitted pulse and b) due to the spread of the signal of the GPR.

1.4.1 Data misrepresentation caused by the transmitted signal (direct wave)

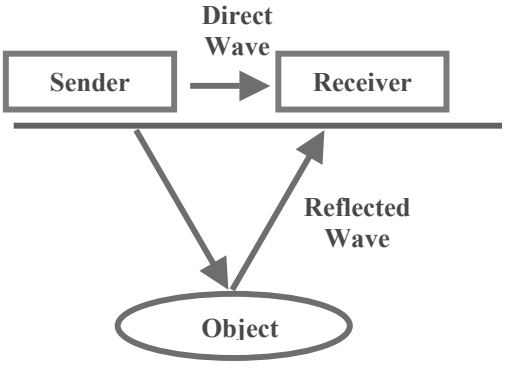

Fig 1.2 Addition of the transmitted signal (direct wave) to the received signals.

The receiver of the GPR not only picks up the signals returned by the different objects but also the direct wave sent out by the transmitter (as shown in Fig 1.2).

The signal of the GPR (direct wave) is not a simple impulse. It appears similar to a Gaussian modulated sine wave. The reflections returned from different objects are proportional to transmitted wave. As the receiver adds the transmitted wave to the returned signals, understanding the structure of the input wave and its behavior is very important. A sample transmitted wave is shown in Fig 1.3.

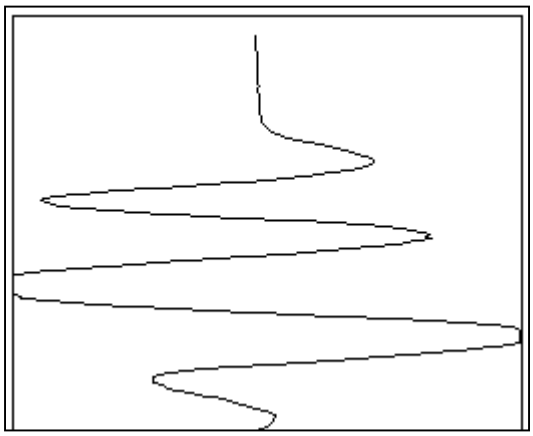

Fig 1.3 Sample Transmitted wave of the GPR.

The alternate positive and negative (left and right) peaks correspond to different intensities of black and white respectively.

The deeper the object, higher the attenuation and lesser the energy that returns. The amount of energy returning mainly depends on the difference in refractive indices at the material boundary.

As the observed image *g* is the result of a convolution between the actual image *f* and the input signal *s*, the relationship is given as

$$g(x, y) = \sum_i f(x, y - i) \times s(i)$$

where *i* denotes the number of elements in the input signal *s*. The *x*-axis denotes the position of the GPR and the *y*-axis denotes time. This convolution is reversed by a technique that uses the linear correlation coefficient, explained in detail in section 5.1.

1.4.2 Data misrepresentation caused by the signal spread

The GPR transmission is not comprised only of signals transmitted vertically, but rather the signal spreads out as a cone emanating from the base of the GPR as shown in Fig 1.4.

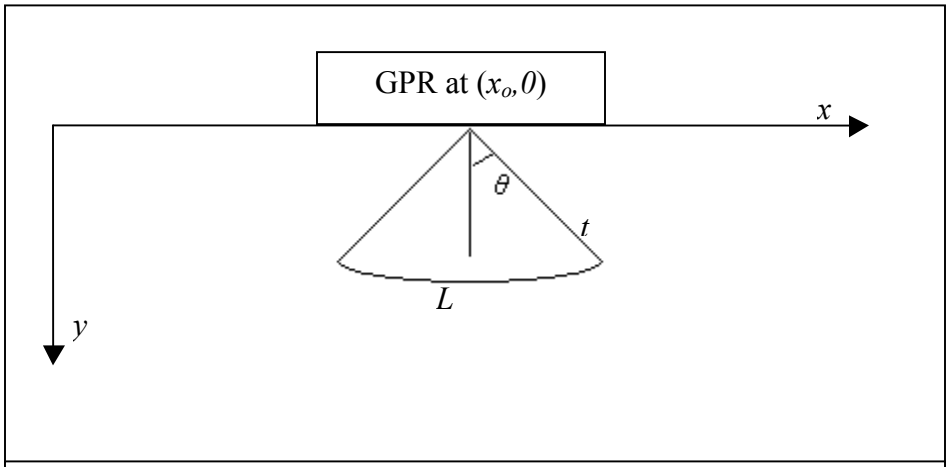

Fig 1.4 Signal Spread of the GPR represented as a cone.

The *x*-axis represents the movement of the GPR (from the left to the right) along the surface and the *y*-axis represents time. The *y*-axis increases in the downward direction. The same definition of the *x* and *y* axes are maintained for all the images of the GPR.

At a particular position, the intensity of wave reflections from the different objects are plotted against the distances of the GPR from these objects. Hence the value of a pixel along the vertical depends on the convolution carried out along the curve of the cone that passes through this pixel.

$$g(x_o, t) = \sum_{-\theta}^{+\theta} f(x, y) h(x_o - x, t)$$

f is the original image, *g* is the measured image and *h* is the kernel The GPR is located at (x_o,*0*) and remains fixed for one measurement. *t* denotes time and θ is the angle of spread. The form of *h* depends on *t,* as *h* is the curve corresponding to a particular value of *t. h* is time-variant. Depth (*y*) and time (*t*) are interrelated. We measure both of them in the same units, pixels. For the arc *L*, all the points lying on the arc are equidistant from the source in terms of time, but not in terms of depth. Hence during our measurements we need to convert time into depth. For a fixed position of the GPR (x_o,*0*), the *x* and *y* coordinates of the different points on the arc are given in terms of time *t* as

$$x = x_0 + t\cos\theta.$$

$$y = t\sin\theta.$$

where θ is the angle of the signal spread. The model shown in Fig 1.4 is explained in detail in section 5.2.

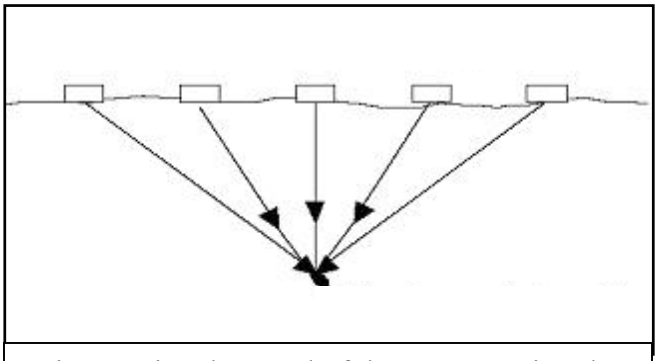

Fig 1.5 Signal Spread of the GPR causing the object to be detected even when not vertically over it.

Due to the signal spread of the GPR as shown in Fig 1.5, a single object appears as a curve (hyperbola) as shown in Fig 1.6.

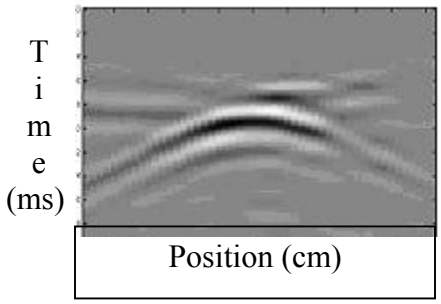

Fig 1.6 Hyperbolic representation of an object caused by the signal spread of the GPR.

The shape and size of the hyperbolae created by objects differ based on the location of the objects. The primary technique used to reconstruct the hyperbolic representations to individual objects is a technique that uses optimization based on gradient descent.

2. LITERATURE REVIEW

GPRs have been used in a variety of applications including mine detection, utility detection and mapping, concrete inspection [11] [19] [21] [23], archaeology [12] [20] [24] [33], structural inspection [2] [6] [10] [15] , geology [1] [16] [17] and mineral detection [8] [9] [28]. Of these, mine detection has been the most popular topic for GPR research. See [5] [27] [35] [36] for some recent survey methods. The main advantage of the GPR over other detectors such as the Electromagnetic Inductor (EMI) is its two dimensional data representation. In addition to the position of the object, this instrument helps determine its depth as well.

2.1 GPR ANTENNA CHARACTERIZATION

According to Radzevicius [26], polarization in wave theory describes the magnitude and direction of electric and magnetic fields with respect to space and time. Two main types of polarization are linear polarization and circular polarization. If waves are linearly polarized, the electric field is directed in a straight line from the transmitter (parallel to each other), whereas in circular polarization the electric vectors emanating from the transmitter are not parallel to each other.

Radzevicius [26] further states that for spherical targets and most linear targets that include pipes and cables, the polarization of the reflected field is independent of the transmitted polarization. However for more general targets, the polarization of the field incident on the receiver antenna is dependent on interference between the polarizations of the transmitter

antenna and those scattering from the targets. Most modern GPRs use dipole or bow tie antennas in which the majority of the electric field is incident (moves along) along the long axis of the bow-tie.

Radzevicius [26] explains that the waves that leave the antenna are called lateral waves and those already present in the area surrounding the GPR are called space waves. The antenna patterns observed are considered to be a result of the interference between these lateral and space waves. However the main factor that defines the antenna pattern is the interaction between the antenna and the lossy dielectric halfspace that is often very close to the GPR. He further suggests that the best method to understand the pattern caused by a short dipole antenna placed near a lossy halfspace is to study the Finite Difference Time Domain (FDTD) model of the signal spread. Maxwell's equations are used to model the electric and magnetic fields of the antenna. FDTD is a method that is used to simulate electromagnetic propagation [32]. As the electric and magnetic fields can be calculated throughout a discretized volume at increasing steps of time, the distribution of the electromagnetic fields can be observed as a function of time. In this case, FDTD was used to replace the spatial and time derivatives in the Maxwell equations with finite difference approximations. His results showed the electric and magnetic fields of the antenna to appear as shown below.

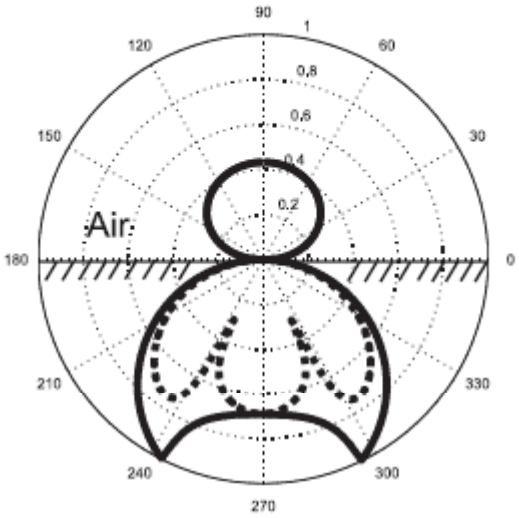

Fig 2.1 Electric (dotted) and Magnetic (dark) patterns for an antenna for a radial scale of 2 wavelengths at 100Mhz, with the source placed very close to the soil surface. From [26]

These lobes, as they are called, caused by the wave interference are heavily dependent on the frequency of the incident wave. Ideally for most applications the radiation pattern should contain a single lobe with most of its energy focused in the downward direction. However in practice, many lobes are created which result in the misrepresentation of data that we observe. Large numbers of lobes are created at higher frequencies, due to rapid interference between lateral and space waves, making data interpretation even more difficult.

Daniels [7] also describes antenna characteristics and the various parameters that are associated with antenna selection. He explains that the major consideration in antenna selection is the target type and that for most common applications the cross-coupled dipole is used as an antenna.

2.2 CATEGORIZATION OF OBJECT RECONSTRUCTION TECHNIQUES

Cardimona [4] categorizes the object reconstruction process from raw GPR data into two parts: “normal processing” and “advanced processing”. Zero time adjust, subtract mean trace and gain adjustment are included in normal processing. Associating zero time with zero depth is called zero time adjust. Superposition of the transmitted wave (direct wave) with the signals received from the ground produces “ringing” or “banding”. A method known a “subtract mean trace”, which is also a high pass filter, is one way of removing this ringing. This method takes the average of a window of pixels and subtracts that average from the value of the pixel that lies in the center of the window. The method is described by the equation shown below

$$g(x,y) = f(x,y) - \frac{1}{m}\sum_{i=-m/2}^{i=m/2} f(x+i,y),$$

where m is the window size. This method and the parameters considered in selecting the window size are described in detail in section 4.2.

Signals that travel less distance and time have greater intensities than the signals that arrive later. Attenuation of these signals is proportional to the time taken for them to propagate. This attenuation is caused due to geometric spreading as well as the absorption of energy by the medium in which the signal propagates. Gain adjustment is required to compensate for the attenuation of the signals.

After the normal or primary processing, advanced techniques can be applied to better interpret the data, most common of which is “migration”. Migration is one term that is used to describe the technique of reconstructing the distorted representation of objects in GPR data (also known as hyperbolae).

The GPR pulse (direct wave) enters the surface and intercepts various irregularities and convolution is the technique that best describes the interaction of this pulse with these irregularities. Deconvolution can be used to remove the effects of the direct wave (shaped like a Gaussian modulated sine wave) to better interpret the GPR image. Inverse filtering is a kind of deconvolution that is commonly used. Inverse filtering involves taking the Fourier transform of the distorted signal and removing the distortion using the frequency domain representation. However, this technique is helpful only when the structure of the source wave is known. The basic approach to inverse filtering using Fourier transforms is shown below.

$$g(t) = f(t) * h(t),$$

where g is the observed distortion of a kernel h over the original image f

In the frequency domain this would be represented as (using discrete time Fourier Transforms)

$$G(k) = F(k) \times H(k).$$

Deconvolution (inverse filtering) of the original image f in the frequency domain is given as

$$F(k) = \frac{G(k)}{H(k)}.$$

F can be converted back into the time domain using the inverse discrete time Fourier transform. As the discrete time Fourier Transform (DTFT) is used to represent a discrete-time non-periodic signal as a superposition of complex sinusoids, the inverse DTFT representation of a time domain signal involves an integral over frequency namely

$$f(t) = \frac{1}{2\pi} \int_{-\pi}^{+\pi} F(k) e^{i\omega k} d\omega$$

2.3 GPRS USED IN MINE DETECTION

Gestel [14], Gader [13] and others have worked extensively in the field of mine detection using GPRs. Gestel [14] implemented migration using a method called "Alford rotation" that analyzes "multi-configurational" data to detect the main orientation of the target. By arranging the receiver and the transmitter in different orientations, data can be recorded in four configurations and hence the term "multi-configurational data". Problems with this method include the requirement to collect data from four angles and the susceptibility of the algorithm to noise. The noise present in real data causes enough disturbance to make the algorithm unstable. Also for accurate location using this method, the radiation patterns of the vertical and horizontal dipoles must be the same, which occurs only in air or extremely homogenous environments.

In [13], Gader uses Hidden Markov Models (HMMs), stochastic models that produce time sequences of random observations as a function of states. This method uses a library

comprised of landmine signatures derived from multiple sources. This library is the main platform for the development of the HMM detection algorithm. Using the proposed HMM technique the algorithm compares a hyperbola with the digital signatures that are present in the library and generates a probability that's associated with the best match for that curve. The HMM technique breaks down the curve into states. Based on the Markov theory that the probability at each state is only dependent on the previous state, a probability is associated with each state. This probability attains an acceptable value only if there is a curve, corresponding to one of the predefined curves, present in the image. The primary disadvantage of this method is the creation of the signature library. In order to achieve a high level of accuracy this library must be continually updated with all the possible signatures from the different objects of interest. Also the various soil types must be taken into consideration.

2.4 RECONSTRUCTIONS BASED ON OPTIMIZATION

Minimization is a technique used very commonly in image restoration algorithms. Hsiao [30] presents a method to determine the ultrasonic reflectivity function resulting from density changes in a medium, which is very similar to the reconstruction of reflections of the electromagnetic waves in GPR systems. Similar to the problem presented in this thesis, this paper estimates the reflected wave as a convolution of the input wave and the reflectivity function of the material. The problem is then reduced to the maximization of a probability that depends on the variation of the measured image from the unknown, and the prior information that best describes the unknown image. This optimization is done using a

technique called “mean field annealing”, that is a type of optimization that attempts to avoid local minima. The technique works well for detecting defects in metallic surfaces, however non-linear reconstructions depend heavily on the prior knowledge of the statistics of the unknown image.

2.5 ALGORITHMS FOR THE INVERSION OF THE TRANSMITTED WAVE

In order to reconstruct the received signals that have been distorted due to the convolution caused by the input wave of the GPR, some models for the transmitted wave have to be constructed. Van der Lijn [34] has presented models for the input wave and analyzed many algorithms to generate the impulse response of targets that would make them easier to classify.

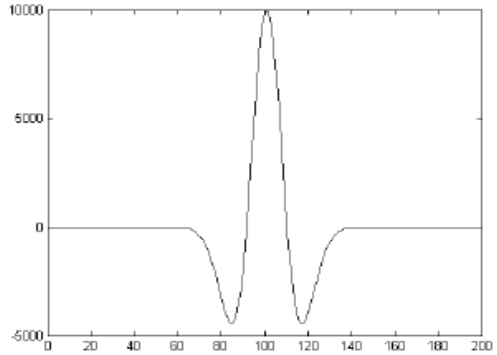

Fig 2.2: The “Ricker Wavelet”. From [34]

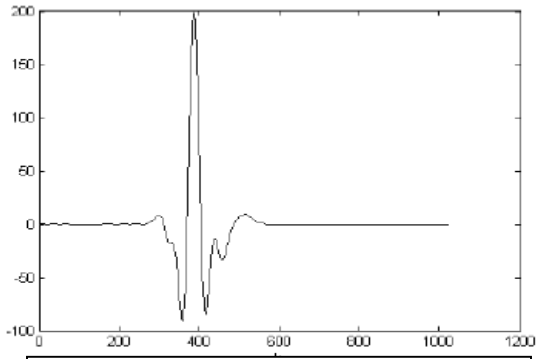

Fig 2.3: The “GPR Wavelet”. From [34]

The impulse response of targets gives information about the size, internal structure and material properties of those targets. In order to obtain the impulse response, many deconvolution algorithms are used. One model used for the GPR wave was the “Ricker

wavelet", shown in figure 2.2, which we observe looks a lot like a Gaussian modulated sine wave. The second model called the "GPR wavelet", figure 2.3, was extracted from an actual GPR signal.

Some of the deconvolution methods employed along with their results are mentioned below.

Deconvolution based on linear least squares uses an error function that is shown below.

$$\min_{g} \| Xg - y \|^2$$

g is an estimate of the impulse response, y is the received signal and the input wave is represented by X.

After experimentation, Van der Lijn [34], showed that this method worked fine for the "GPR wavelet" but not for the "Ricker wavelet". This occurred as to the structure of the "Ricker wavelet" was smooth with most values being neighbor-dependent unlike the "GPR wavelet" which had values are independent of its neighbors. The least squares method seems to work better for waves that had values independent of each other.

A variant of the above method called "ridge regression" is shown below.

$$\min_{g}(\| Xg - y \|_2^2 + \lambda \| g \|_2^2)$$

The second term calculates the squared second norm of g. This term helps improve the noise sensitivity during the inversion. The sensitivity to noise is determined by the choice of λ, which if chosen large, handles large disturbances but increases errors in the primary

reconstruction. Hence a λ must be selected that provides effective noise reduction and acceptable errors in the reconstruction.

Van der Lijn [34] also states that by exploiting the structure of the impulse response of the target, the sensitivity of the deconvolution algorithm to external disturbances could be reduced. Also only part of the input wave (depending on the type of the wave to decide which part) plays an important role in the calculation of the output. Hence Van der Lijn [34] has presented a method called "subset selection using single columns" (SSUSC), which only tries to use the relevant parts of the input and output waves to help in the reconstruction. The main advantage of this method is its speed of execution. However, it does require prior knowledge of the exact shape of the impulse response. Van der Lijn concludes that this is one of the best deconvolution algorithms and improves on this by presenting variants that help better determine or select the portions of the wave that need to be dropped.

2.6 MIGRATION ALGORITHMS

Herman [18] presents an approach that is quite similar to the one we use based on our Ramac GPR. After eliminating the transmitted wave using a background removal scheme, a migration technique called "coherent summation migration" is used to relocate the actual data. This method called *volume based processing*, uses a summation technique about the neighborhood of a particular location.

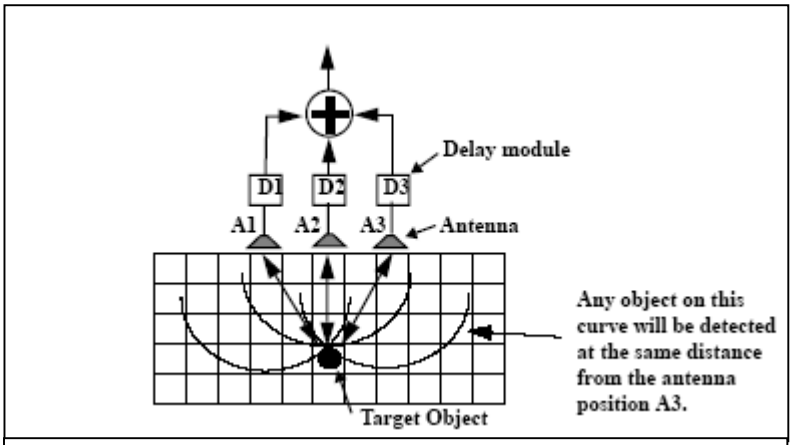

Fig 2.4: Coherent Summation. From [18]

The principle states that the summation would result in a constructive interference only at the real locations of the objects and destructive interference elsewhere. An appropriate threshold decides the presence or absence of an object. The major advantage of this method is that it can begin even before the data collection is complete.

Herman [18] also describes an alternate method called "surface based GPR processing" based on template matching that reduces 3D data into 2.5 D. 3D data contains a lot of information about the soil and the object, some of which might not be required to detect objects. The transmitted signal of the GPR is structured such that most of the information from the returned waves is contained at those points of the wave that correspond to large amplitude or phase changes. Herman states that most of the information in a single received signal is present at the points where the phase of the wave changes, i.e. the peaks. By passing

the wave through a peak detector, only the peaks remain and the rest of the data is neglected. This could possibly reduce the number of data points to be observed by a scale of 200. This new grid of data that only has values at the peaks of the signal is called “2.5 D” data or a “range image”. By observing the amplitudes of the peaks for the various objects at the different depths, Herman [18] used template matching and thresholding to detect objects.

Volume based processing is generally poor at handling soil heterogeneities, and requires an accurate estimate of the velocity in the medium. Surface based processing, on the other hand, handles soil heterogeneities pretty well, does not require accurate velocity estimates.

3. OPTIMIZATION ALGORITHM

The common algorithm used to invert the distortions produced by the transmitted signal of the GPR is a technique based on the optimization of an objective function. This objective function is created by a combination of the data present in the received signal and the known characteristics of the actual undistorted signal. This function is optimized using a technique called mean field annealing which uses gradient descent.

3.1 CONSTRUCTING THE OBJECTIVE FUNCTION

In this section I follow the terminology used in [30]. For ease of understanding, we initially represent the two-dimensional reflectivity function *f(x,y)* as if it were a one-dimensional signal *f(t)*. The transformation to two-dimensions is straightforward.

For a linear, time invariant system, we model the generation of the measured signal by the convolution of an unknown reflectivity function *f(t)* with a kernel *h(t)* and the result, *g(t)* is given as,

$$g(t) = f(t) \otimes h(t). \qquad 3.1$$

The above equation, however does not consider noise. Assuming that the noise is additive, the system is described as shown below

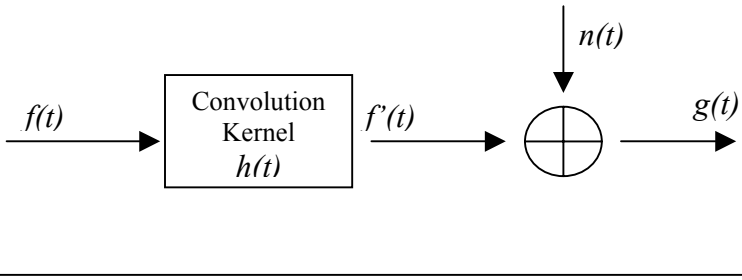

Fig 3.1 Flow Diagram of the system.

f'(t) is the result of the initial distortion and *n(t)* is the noise.

$$f'(t) = f(t) \otimes h(t), \qquad 3.2$$

where $\otimes$ denotes convolution.

Hence the noise *n* is given as

$$n(t) = g(t) - f'(t). \qquad 3.3$$

As the noise is assumed additive and the probability of noise is assumed Gaussian, then denoting probability density by *p*,

$$p(n) = \frac{1}{\sqrt{2\pi}\sigma} e^{\frac{-n^2}{2\sigma^2}}. \qquad 3.4$$

From the above equation we extend the formulation to the two-dimensional case, where we consider the received signal as a two-dimensional array of pixels. We enumerate a single pixel (*i*) as a lexicographic representation such that each pixel has a unique index *i*(*x*,*y*). In terms of pixel *i*, the above equation is given as

$$p(g_i - f_i') = \frac{1}{\sqrt{2\pi}\sigma} e^{\frac{-(g_i - f_i')^2}{2\sigma^2}}. \qquad 3.5$$

The above equation defines a probability specific to the value of a pixel in the image. As the only difference between *f'* and *g* is the noise, the probability of noise is the probability of (*g*

– f') and thus is also the conditional probability density $p(g \mid f)$ that the observed image g was generated by f. Hence

$$p(g_i \mid f_i) = \frac{1}{\sqrt{2\pi}\sigma} e^{\frac{-(g_i - f_i')^2}{2\sigma^2}}. \qquad 3.6$$

Noise is assumed to be an independent random process and thus the probability density of generating the entire image f give the probability density of image g is given as

$$p(g \mid f) = \prod_i p(g_i \mid f_i). \qquad 3.7$$

$$p(g \mid f) = \prod_i \frac{1}{\sqrt{2\pi}\sigma} e^{\frac{-(f_i' - g_i)^2}{2\sigma^2}} \qquad 3.8$$

In order to convert this probability into one that denotes the probability density of f, given the measured image g, $p(f \mid g)$ we use Bayes' rule

$$p(f \mid g) = \frac{p(g \mid f) * p(f)}{Z}. \qquad 3.9$$

Where Z is simply a normalization constant that does not depend on the estimated image f. $p(f)$ constitutes a term called the "prior" that contains features and properties of the original image.

Hence in order to reconstruct the image, we find the image f such that $p(f \mid g)$ is maximized. This approach is called the maximum a posteriori (MAP) approach. By taking the logarithm and changing the signs from equation 3.9 we convert the problem from a maximization to the minimization of an objective function.

$$H(F) = \sum_i \frac{(f_i' - g_i)^2}{\sigma^2} + \sum_i (\Lambda(f_i)). \qquad 3.10$$

$H_n = \sum_i \frac{(f_i' - g_i)^2}{\sigma^2}$ is called the "noise" term and $H_p = \sum_i (\Lambda(f_i))$ is called the "prior" term.

The "prior" term denotes the features in the image that need to be enhanced. Properties of an image such as edginess, blur and brightness can be components of the prior. Based on numerous experiments [3, 30, 31], it was discovered that an appropriate prior would be

$$H_p = \frac{-1}{\sqrt{2\pi}\tau} \sum_i e^{\frac{-(f \otimes r)_i^2}{2\tau^2}}. \qquad 3.11$$

where r is a kernel which estimates the first derivative. Such a kernel finds solution images that are smooth, but which retain sharp edges.

3.2 GRADIENT DESCENT

"Gradient Descent" is a minimization scheme uses and objective function and attempts to find its solution by moving in the direction opposite to the slope of that function given by the equation below.

$$f_l^{k+1} = f_l^k - \alpha \frac{\partial H^k}{\partial f_l}, \qquad 3.12$$

where H is the objective function (in our case either H_n or H_p), k is the iteration number, f_l is one element of the vector representation of the image f and α, the "step size", is a constant to ensure that only small steps are taken in the direction of the minima.

In order to apply gradient descent, the energy function must be differentiated. After differentiating the noise term from Eq 3.10, we get

$$\frac{\partial H_n}{\partial f_i} = \frac{1}{\sigma^2}[(f \otimes h)_i - g_i] \otimes h_{rev} \qquad 3.13$$

where h_{rev} is the reverse of the original kernel h. In order to explain the differentiation of a convolution we use a 1-D model in which f_i is a pixel from the original image, g_i is a pixel from the measured image and h is a kernel with three elements in it ($h_{-1}h_0h_{+1}$). Hence we write out the terms involving a pixel f_3 at which a measurement g_3 was made in the noise term from Eq 3.10.

$$\begin{aligned} H_n &= ((f \otimes h)_2 - g_2)^2 + ((f \otimes h)_3 - g_3)^2 + ((f \otimes h)_4 - g_4)^2 \\ &= (f_1 h_{-1} + f_2 h_0 + f_3 h_{+1} - g_2)^2 \\ &+ (f_2 h_{-1} + f_3 h_0 + f_4 h_{+1} - g_3)^2 \\ &+ (f_3 h_{-1} + f_4 h_0 + f_5 h_{+1} - g_4)^2 \end{aligned} \qquad 3.14$$

When H_n from the equation above is differentiated with respect to pixel f_3 all the terms that don't contain that pixel reduce to zero and the result looks something like this

$$\begin{aligned} \frac{\partial H_n}{\partial f_3} &= 2((f \otimes h)_2 - g_2)h_{+1} + 2((f \otimes h)_3 - g_3)h_0 + 2((f \otimes h)_4 - g_4)h_{-1} \\ &= 2(((f \otimes h) - g) \otimes h_{rev})_3 \end{aligned} \qquad 3.15$$

where $h_{rev} = h_{+1}h_0h_{-1}$ and $(f \otimes h) - g)$ is computed at all points where g_3 is measured. Hence h_{rev} is just the kernel h reversed.

Similarly differentiating the prior term from Eq. 3.11 we get,

$$\frac{\partial H_p}{\partial f_i} = \frac{1}{2\sqrt{2\pi}\tau^3}[(f \otimes r)_i \cdot e^{\frac{-(f \otimes r)_i^2}{2\tau^2}}] \otimes r_{rev}. \qquad 3.14$$

where r_{rev} is the reverse of the kernel r and follows the same explanation as h_{rev}. The combined minimization function becomes

$$\frac{\partial H}{\partial f} = \frac{\partial H_n}{\partial f} + \frac{\partial H_p}{\partial f}. \qquad 3.15$$

3.3 MEAN FIELD ANNEALING

A very common method of optimization is simulated annealing (SA). Simulated annealing is a global optimization technique that primarily attempts to distinguish between different local minima. The algorithm starts from an initial point, takes a step and evaluates the function. Normally, during a minimization most downhill steps are accepted and the process continues from the new point. The main characteristic of this algorithm is that in an attempt to avoid local minima it might accept an uphill step. As the number of iterations of the algorithm increase, the length of the steps taken tend to decline and the algorithm begins to converge on a global optimum. This algorithm is considered to be robust as it makes very few assumptions about the function to be optimized. This method however could take 10 to 1000 times the computing time compared to simpler optimization techniques.

To improve the search we introduced “mean field annealing” (MFA), which retains some of the potency of the simulated annealing (SA) algorithm, but replaces random searches by a series of deterministic gradient descents. It avoids most local minima and provides solutions to optimization problems that are nearly global.

In MFA [3], [29] the τ in the prior term is initially set to a very high value such that the prior term is zero at the start of the gradient descent algorithm. τ is then decreased gradually making the prior term more and more significant. This approach runs dramatically faster than SA and is shown to arrive at a nearly global minimum, given sufficient time.

4. PRIMARY PROCESSING OF THE RECEIVED GPR SIGNAL

The raw data from the GPR is illustrated in Fig 4.1. The *x*-axis represents the motion of the GPR along the surface and the *y*-axis (increasing downwards) indicates time.

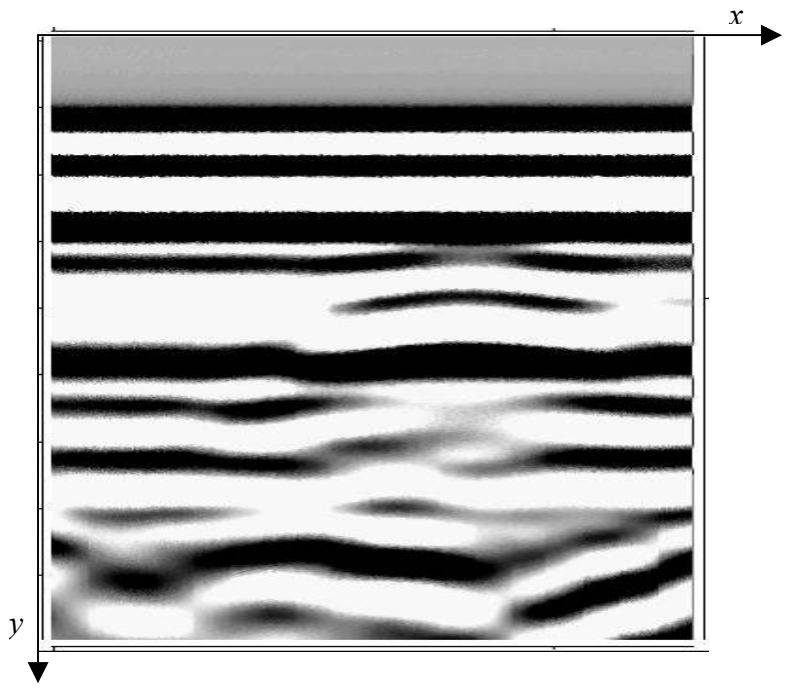

Fig 4.1 Raw Data from the GPR

From this initial GPR image the reconstruction or object extraction process constitutes two main steps.

a) Background Removal.

b) Data Migration.

   i) Correlation of the transmitted signal

   ii) Antenna signal spread.

After these two steps, post-processing includes steps such as thresholding and object extraction.

4.1 BACKGROUND REMOVAL BASED ON "SUBTRACT TRANSMITTED PULSE"

The received data contains the "direct wave", the reflected waves and external noise. The instrument is designed such that the receiver continues to listen even as the transmitter sends out the pulses. This effect is primarily due to the close proximity of the transmitting and receiving antennae. As a result, the receiver picks up the transmitted wave and superimposes it on the reflected signals. Since the transmitted signal is strong due to the close proximity of the antenna to the receiver, it is very bright and thus it is difficult to identify gradients in the image. The transmitted wave must be removed. There are two methods that were used to do this, a) using a sample transmitted pulse and b) subtracting the mean trace.

In the "Subtract Transmitted Pulse" method, a sample pulse is subtracted from the entire image. This sample pulse is extracted from GPR data recorded in an empty environment. The running time of this algorithm is $\theta(n)$, where n is the number of pixels. Though quick, this algorithm does not consider the dynamic nature of the working environment, and hence at times the sample input wave does not exactly coincide with the actual wave used in practice. This method leaves heavy traces of the input signal that are considered as anomalies by the migration algorithm. A sample input image and its filtered output are shown in Fig 4.2.1 and Fig 4.2.2.

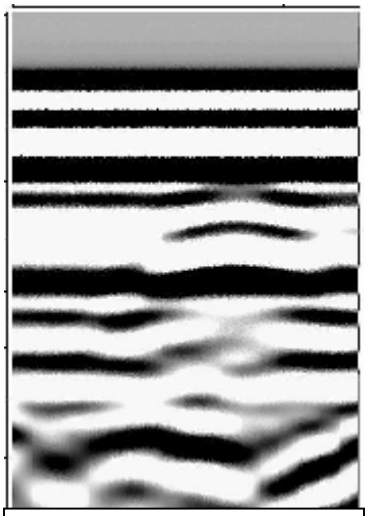

Fig 4.2.1. Initial Data.

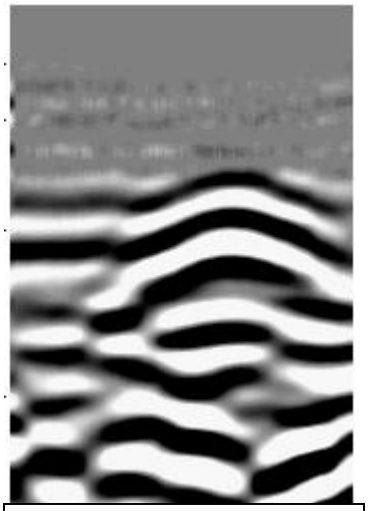

Fig 4.2.2. Filtered Result from the "Subtract Transmitted Pulse" method.

This technique only considers the transmitted signal and does not eliminate any external noise.

4.2 BACKGROUND REMOVAL BASED ON "SUBTRACT MEAN TRACE"

In this method we define a window of around 30 – 40 pixels and subtract from all the pixels in this window the mean of the pixels in it. The window is moved along and the procedure is repeated until the entire image is covered, as given in Equation 4.1.

$$g(x,y) = f(x,y) - \frac{1}{m}\sum_{i=-m/2}^{i=m/2} f(x+i,y) \qquad 4.1$$

where f represents raw data, g the filtered image and m is the window size.

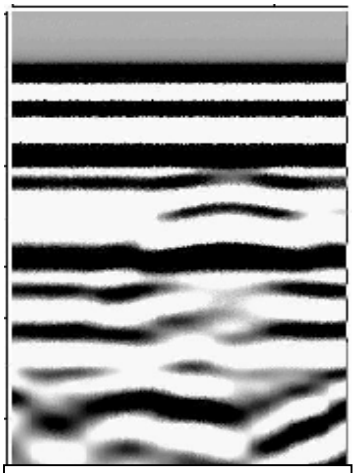

Fig 4.3.1. Initial Data.



Fig 4.3.2. Filtered Result using the "Subtract Mean Trace" method.

This method does not require any prior knowledge of the GPR signal. The running time of this algorithm is the window size multiplied by the previous method. As a result, selection of a large window requires more processing time, which is critical in real time applications. A sample input image and its filtered output are shown in Fig 4.4.1 and Fig 4.4.2.

Running time (Subtract Mean Trace) = m * Running time (Subtract transmitted pulse)



Fig 4.4.1. Window size - 30

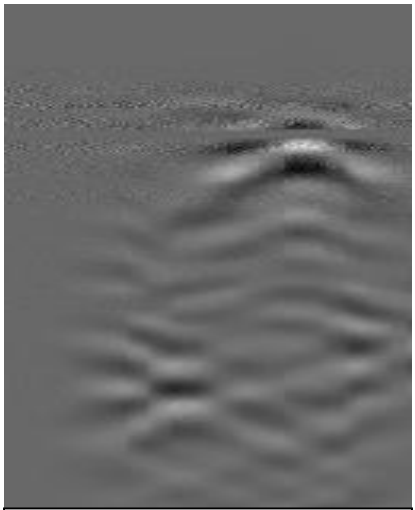

Fig 4.4.2. Window Size - 200.

Sample filtered images for window sizes 30 and 200 pixels are shown in Fig 4.4.1 and Fig 4.4.2 respectively. After experimentation, the optimum window size was found to be between 30 – 40 pixels.

5. DATA MIGRATION

5.1 CORRELATION OF THE TRANSMITTED SIGNAL

5.1.1 Signal Description and Simulation

The transmitted pulse (direct wave) of the GPR is not an impulse. It rather resembles a Gaussian modulated sine wave (as shown in Fig 5.1). As a result, the reflections returning from different objects are varying magnitudes of this wave.

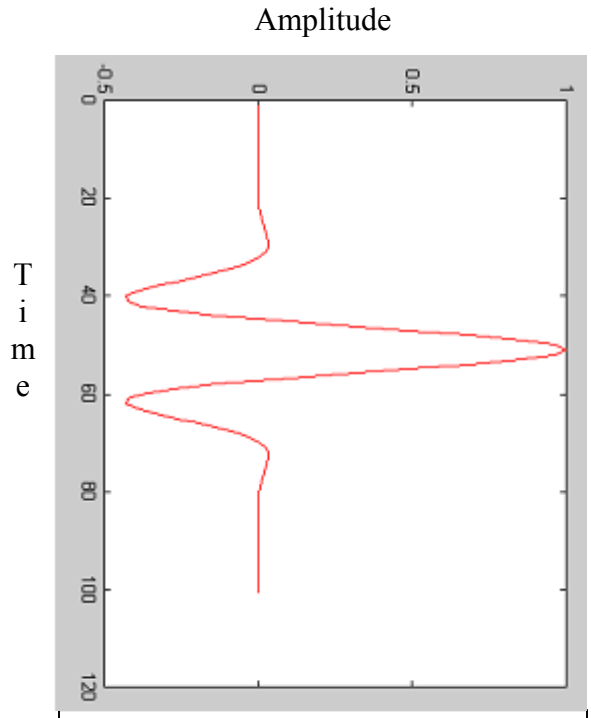

Fig 5.1 Transmitted signal modeled by a Gaussian modulated sine wave (Signal *S*)

As the observed image *g* is the result of a convolution between the actual image *f* and the input signal *s*, the relationship is given as

$$g(x,y) = \sum_i f(x, y-i) \times s(i)$$

where i denotes the number of elements in the input signal s. The x-axis denotes the position of the GPR and the y-axis denotes time.

In order to obtain an optimum algorithm for the reconstruction, we initially simulate a GPR image in order to have a better control over the algorithm development. Once an algorithm is designed, the method is extended to actual data from the GPR.

The simulation of a disc placed under the ground surface is shown in Fig 5.2. The horizontal axis represents the line along which the GPR moves and the vertical axis denotes the depth of the object. Only the upper half of the disc is considered.

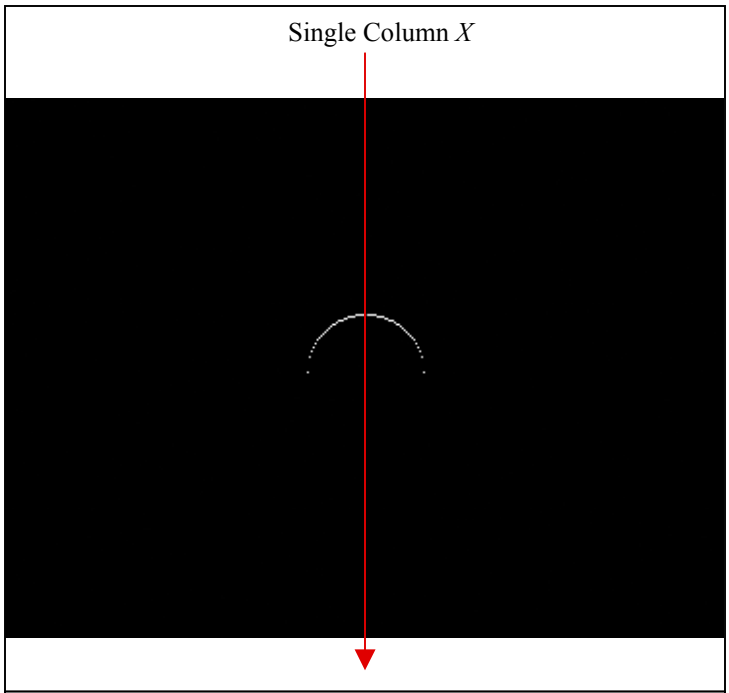

Fig 5.2 Simulated image of a disk placed under the ground surface

When the transmitted wave (*S*) as modeled in Fig 5.1 is reflected in part from the circular disk as shown in Fig 5.2, the signals received by the GPR appear as shown in Fig 5.3. Each part of the disk reflects a certain amplitude of the direct wave.

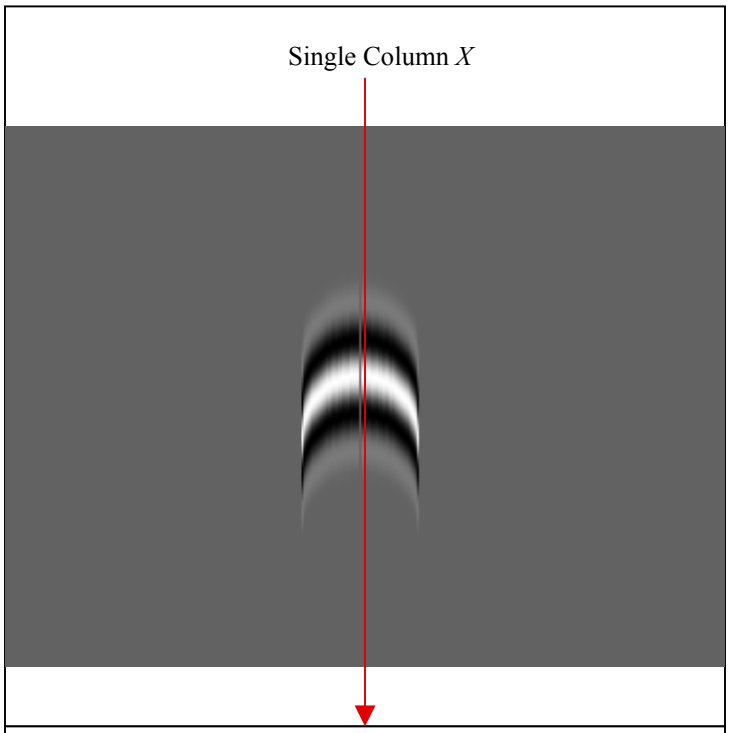

Fig 5.3 Received image from the GPR (Simulated).

5.1.2 Linear Correlation Coefficient (LCC)

The linear correlation coefficient (*r*) is a quantity that determines the relationship between two functions. Its value ranges from –1 to +1. +1 indicates a direct relationship between the two functions, 0 indicates no relationship and –1 indicates an inverse relationship. The square of this coefficient, r^2, also known as the coefficient of determination, determines the variance between the two functions. Mathematically *r* is defined as

$$r_{xy} \equiv \frac{\sum_{i=1}^{n}(x_i - \bar{x})(y_i - \bar{y})}{\sqrt{\sum_{i=1}^{n}(x_i - \bar{x})^2 \sum_{i=1}^{n}(y_i - \bar{y})^2}} \qquad 5.1$$

where x and y are the two functions with n values each.

$\bar{x}$ is the mean value of x defined as $\frac{1}{n}\sum_{i=1}^{n} x_i$ and $\bar{y}$ is the mean value of y defined as $\frac{1}{n}\sum_{i=1}^{n} y_i$.

In order to reverse the correlation caused by the transmitted wave, we isolate the returned image (Fig 5.3) into individual columns. This can be done assuming that the result of the correlation in a single column (one particular position of the GPR) is independent of the data present in the remainder of the image. Hence we have now reduced the problem to a reconstruction in one dimension.

If we consider the column corresponding to the center of the circular disc (Column *X*) in Fig 5.2, we observe a pattern as shown below.

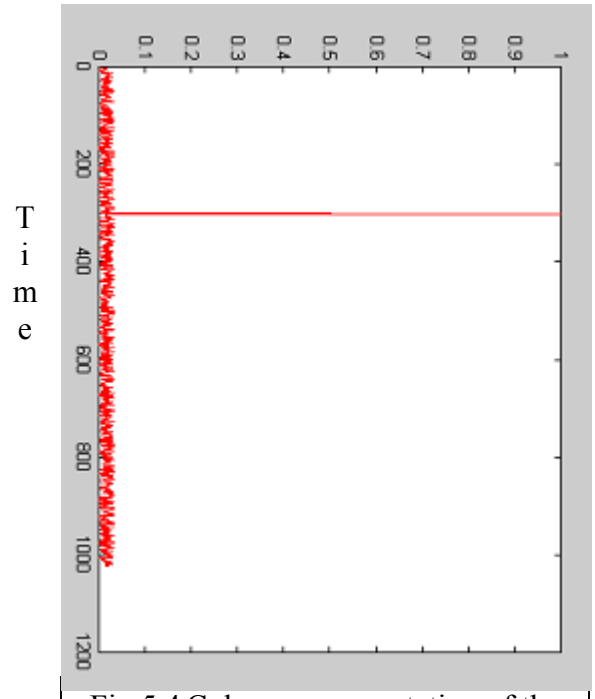

Fig 5.4 Column representation of the center of the disk. (Column *X*)

The impulse in the above figure corresponds to the bright spot on the disc, which was roughly at a depth (position) of 300 pixels. In order to avoid the unreasonable case of a homogenous background, we added Gaussian noise with a standard deviation of 0.1 to all the remaining pixels that comprised the soil beneath the surface. The result of the correlation between the input pulse (*S*) and the Column *X* is shown below (Column *Y*).

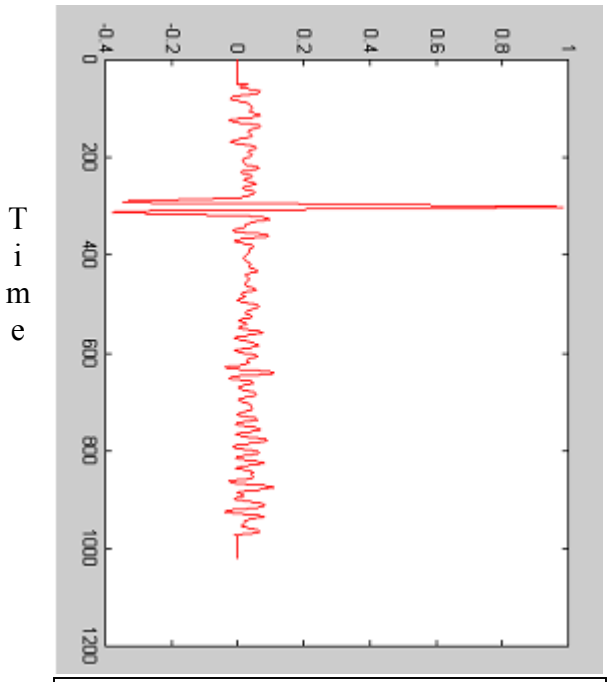

Fig 5.5 Result of the Correlation.
(Column *Y*)

In order to invert the correlation we use the linear correlation coefficient (*r*) from Eq. 5.1. The pseudocode for the calculation of *r* is shown below.

for j = 51 to (1000 – 51) do (no of elements in a single column)

R[j] = 0.0;

for n = -50 to +50 do (101 elements in the input signal S)

R[j] += Y[j + n] x S[50 + n].

As the input signal *S* contains 101 elements, *n* in this equation is set to 101. To calculate *r* at a particular pixel (*i*) from Column *Y*, we need to select 101 elements including pixel *i*. We do this by selecting *i* as the 51st element and completing the array of 101 by taking 50 continuous elements from either side of *i*. This process has to be repeated 1000 times to calculate *r* for each of the 1000 elements in Column Y. Due to the method of selection of the

101 elements, there are 50 pixels at the beginning and 50 pixels at the end of Column *Y* that do not have a value.

The linear correlation coefficient r_{SY} for the elements in Column *Y* with the input signal *S* is shown below.

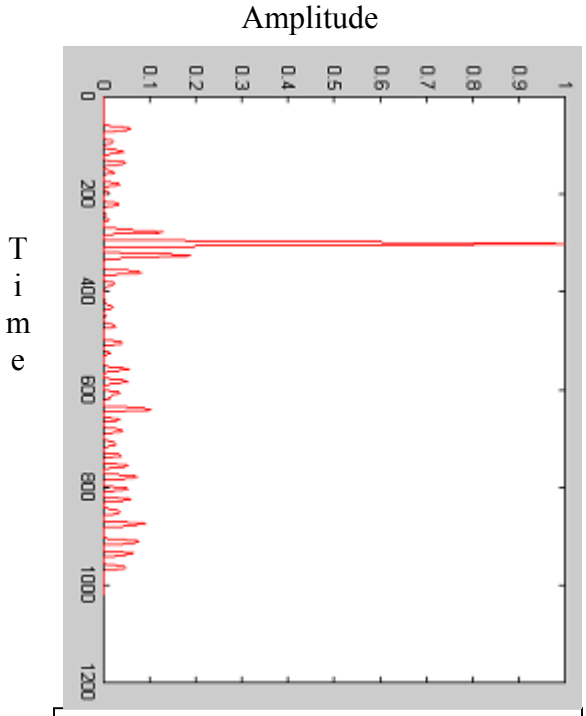

Fig 5.6 Reconstructed image - Linear Correlation Coefficient r_{SY} (Column *F*).

As negative values of *r* indicates inverse relationships, we ignore all negative values of *r*. Our simulation assumes that there can only be one object in a particular column, i.e. there cannot be two objects one below the other. Hence there can only be one bright spot in one column. In the above image (Column *F*), this maximum value (1.0 in this case, which indicates a perfect direct relationship) is found to be at the 300th position, which is exactly

where we had the bright spot originally (Column *X*). Consequentially, the maximum value of each column should correspond to an object. This however is not the case, as only the maximum value of each column that is greater than a particular threshold value represents an object.

In practice it was observed that even though the filtered images of actual GPR data (Fig 4.4) do not have perfect discs or features as shown in Fig 5.2, but rather hyperbolic representations of these objects, the correlation of the input signal results in an image which contains columns that are independent of each other. Hence the linear correlation coefficient method can be applied successfully without any modifications.

In order to implement the above algorithm to real data, an iron pipe 25 inches in length and 7 inches in diameter was placed 15 inches deep in a sandbox. The pipe was kept perpendicular to the line of motion of the GPR. The soil used in this experiment was dry sand.

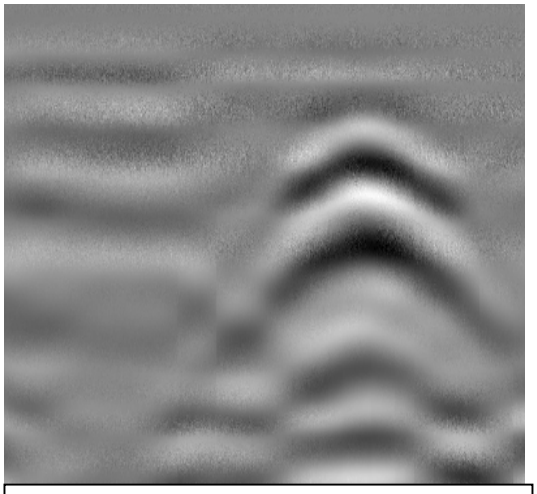

Fig 5.7 Filtered image of actual data from the GPR.

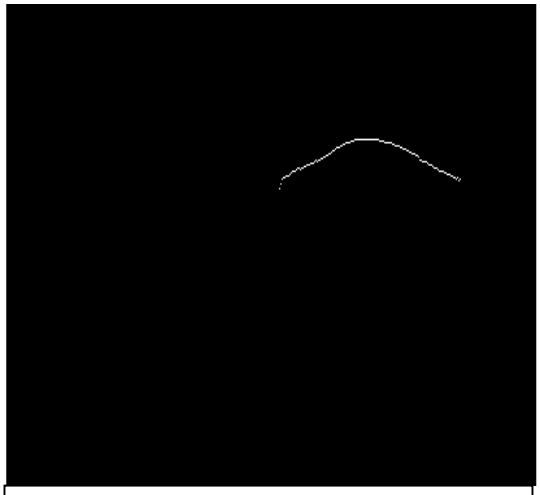

Fig 5.8 Result of the LCC technique applied to Fig 5.7.

Fig 5.7 shows the filtered result of the measurement. When the LCC technique is applied to this image, the result after thresholding is shown in Fig 5.8. The input signal *S* used in this case is the actual wave of the GPR, which is shown in Fig 1.2. The original image comprised of 923 columns and 1024 rows. The algorithm took approximately18 seconds to run on a Pentium 4 2000. Hence, as the reconstruction resembles a hyperbola with a dark background, it can be reduced to its original form using the technique presented in Section 5.2.

5.2 ANTENNA SIGNAL SPREAD

In order to reconstruct the hyperbolae caused due to the signal spread of the GPR, we construct an objective function as explained in Chapter 3 and attempt to optimize it such that it converges to one particular solution based on certain parameters of the original image that we shall define. As explained the objective function comprises of two terms, the noise term and the prior term. The parameters of the original image are incorporated in the prior term.

5.2.1 Incorporating the Prior and Noise Terms

A model was created to simulate the signal spread of the antenna. A circular disc was used as the object of choice.

Noise term

Originally the noise term H_n (from Eq 3.10) looks like

$$H_n = \sum_i \frac{(f_i' - g_i)^2}{\sigma^2} \qquad 5.2$$

This equation was differentiated to be included in the minimization of the objective function. It then takes the form (from Eq. 3.13)

$$\frac{\partial H_n}{\partial f_i} = \frac{1}{\sigma^2}[(f \otimes h)_i - g_i] \otimes h_{rev}. \qquad 5.3$$

where h represents the kernel to be applied and h_{rev} represents the reverse of this kernel.

We have to construct the kernel (h) that models the antenna spread. The model of the signal spread is shown in Fig 5.9. From experimental observations we have concluded that the spread angle of the GPR is modeled (as best described by literature and experimentation) to be around 45 degrees. Also, the wave front is assumed to be circular. We model the signal spread in two dimensions and hence the wave appears as a sector subtended at an angle of 45 degrees on either side of the normal to the GPR. Effectively we get a sector with a radius corresponding to the depth and a total angle of 90 degrees. The kernel (h) is effectively the outer arc of this sector, the arc length of which is calculated from the parameters discussed above.

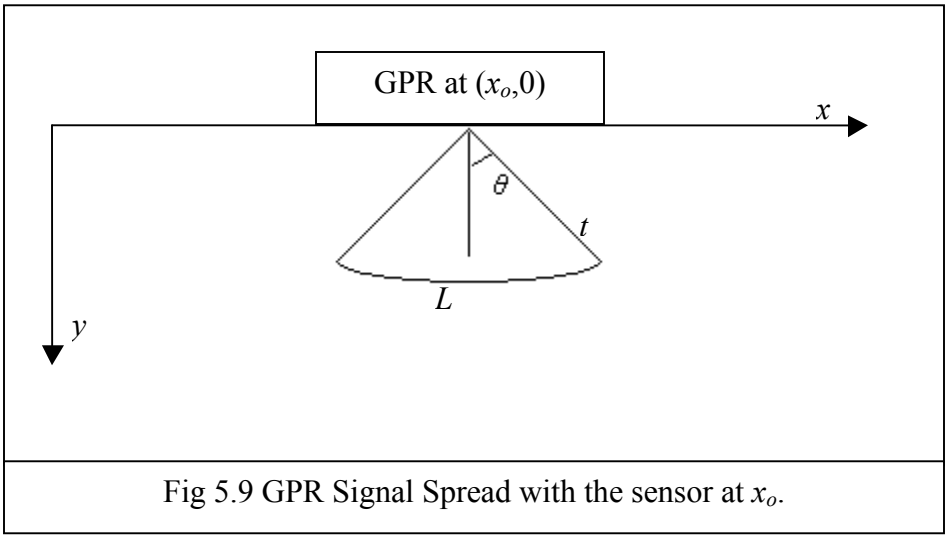

Fig 5.9 GPR Signal Spread with the sensor at x_o.

The position of the GPR is given by (x_o,0). y signifies depth and increases in the downward direction.

In the 2-dimensional – x,y - case we model the signal generation process as

$$g(x_o, t) = \sum_{-\theta}^{+\theta} f(x, y) h(x_o - x, t)$$

f is the original image, g is the measured image and h is the kernel The GPR is located at (x_o,0) and remains fixed for one measurement. t denotes time and θ is the angle of spread. The form of h depends on t, as h is the curve corresponding to a particular value of t. h is time-variant. Depth (y) and time (t) are interrelated. We measure both of them in the same units, pixels. For the arc L, all the points lying on the arc are equidistant from the source in terms of time, but not in terms of depth. Hence during our measurements we need to convert time into depth. For a fixed position of the GPR (x_o,0), the x and y coordinates of the different points on the arc are given in terms of time t as

$$x = x_0 + t\cos\theta.$$

$$y = t\sin\theta.$$

where θ is the angle of the signal spread.

The simulation moves the signal source from one end of the image to another. At each position of the signal source, for different times (pixels), we calculate the arc length and apply that as a kernel to the image at that pixel (same as equation 5.4). We store the result for each pixel in an array (another image). This process is repeated for the next position of the signal source and so on until the end of the image.

The signal is considered to be at its strongest down the center of the cone and attenuates gradually away from the center. The signal of the GPR attenuates heavily as it propagates deeper into the surface. The simulation incorporates this using an attenuation parameter that moderately models that of the GPR. Experimentation with objects placed at different depths the yielded the following results.

Original Strength of the signal / Response from an object 100 pixels deep = 113.

Original Strength of the signal / Response from an object 500 pixels deep = 527.

These responses however were from objects placed in dry sand. For wet clay the signal strengths drop down by a further one third due to the refractive index of wet clay. Since the medium of observation for all the experiments was chosen as dry sand we choose an approximate attenuation parameter of 1/t where, where $t \neq 0$, corresponds to the object depth in pixels.

In order to reverse of the kernel (outer kernel in Eq 5.3), the same process is repeated with an inverted kernel. The kernel is inverted about the y-axis, i.e. we take a mirror image of the arc that we used before and apply it to the result of the above operation.

Prior term

In Eq 3.11 we defined the prior term H_p as

$$H_p = \frac{-1}{\sqrt{2\pi}\tau} \sum_i e^{\frac{-(f \otimes r)_i^2}{2\tau^2}}. \qquad 5.5$$

and in the minimization equation (from 3.16) as

$$\frac{\partial H_p}{\partial f_i} = \frac{1}{2\sqrt{2\pi}\tau^3}[(f \otimes r)_i \cdot e^{\frac{-(f\otimes r)_i^2}{2\tau^2}}] \otimes r_{rev} .. \qquad 5.6$$

In order to incorporate a prior term we need to possess some knowledge of the original image before it was distorted. In this case we know that the original image comprises a bright disc kept in a dark background. In case of actual GPR data, the filtered and reconstructed image (from section 5.1) is supposed to have bright curves corresponding to the edges of the different objects against a dark background. Hence the prior term we selected smoothes the image (in order to eliminate noise) while preserving the strong edges (which correspond to the outline of the disc). We model the prior term as piecewise linear, which means that we assume that the model consists of segments that are planar (considering that the intensity as a function of x and y is a plane). This model has been used effectively in [3], [31]. A planar form results if one chooses to minimize the effects of the second derivatives. Thus following [3] [31] we define the prior with the help of three kernels.

$$\Delta_{xx} = \frac{1}{\sqrt{6}}\begin{bmatrix} 0 & 0 & 0 \\ 1 & -2 & 1 \\ 0 & 0 & 0 \end{bmatrix},\ \Delta_{yy} = \frac{1}{\sqrt{6}}\begin{bmatrix} 0 & 1 & 0 \\ 0 & -2 & 0 \\ 0 & 1 & 0 \end{bmatrix},\ \Delta_{xy} = 2\begin{bmatrix} -0.25 & 0 & 0.25 \\ 0 & 0 & 0 \\ 0.25 & 0 & -0.25 \end{bmatrix}$$

Δ_{xx} is a kernel which when applied to image f approximates $\frac{\partial^2 f}{\partial x^2}$. Similarly Δ_{yy} approximates $\frac{\partial^2 f}{\partial y^2}$ and Δ_{xy} approximates $\frac{\partial^2 f}{\partial xy}$.

In order to identify edges about a particular pixel we place the kernel over it. As a result the center of the matrix corresponds to that pixel and the 8 values around it map the 8 neighbors of that pixel (except at the corners of the image). The magnitudes of the pixel and its

neighbors are multiplied by the respective values in the matrix. The magnitude of this result is proportional to the edge strength of that pixel.

As shown in Eq 3.14 and Eq 3.15, after the prior term is differentiated, the result of the first convolution (with r) is further convolved with the reverse of the kernel (r_{rev}) used for the first convolution. Before we apply the reverse kernel we take the results of the three kernels applied to the image ($f \otimes r$) and use them in the exponential in equation 5.5. These values are stored separately. Next, we perform the second convolution (with r_{rev}) using the three results. The kernels for r_{rev} are shown below. Notice that due to their symmetry only the form of Δ_{xy} changes.

$$\Delta_{xx} = \frac{1}{\sqrt{6}}\begin{bmatrix} 0 & 0 & 0 \\ 1 & -2 & 1 \\ 0 & 0 & 0 \end{bmatrix},\ \Delta_{yy} = \frac{1}{\sqrt{6}}\begin{bmatrix} 0 & 1 & 0 \\ 0 & -2 & 0 \\ 0 & 1 & 0 \end{bmatrix},\ \Delta_{xy} = 2\begin{bmatrix} 0.25 & 0 & -0.25 \\ 0 & 0 & 0 \\ -0.25 & 0 & 0.25 \end{bmatrix}$$

These values are then used to create the prior term that is added with the noise term to give us the derivative of the objective (H) function.

5.2.2 Gradient Descent and the MFA Algorithm

The gradient descent equation is given as

$$f_l^{k+1} = f_l^k - \alpha \frac{\partial H^k}{\partial f_l}, \qquad 5.7$$

where H is the objective function (in our case either H_n or H_p), k is the iteration number, f_l is one element of the vector representation of the image f and α, the "step size", is a constant to ensure that only small steps are taken in the direction of the minima.

The image obtained after the filtering and the reconstruction from section 5.1 is used as the initial estimate in equation 5.7. This image is used in the noise and the prior terms to get the difference $\frac{\partial H}{\partial f}$. This difference is multiplied by α and subtracted from the initial estimate. This becomes the input image for the next iteration of the gradient descent and so on till we arrive at an estimate that does not produce a sizeable change in the term $\frac{\partial H}{\partial f}$.

MFA is incorporated by setting the τ in the prior term to a very large value initially. This makes the prior term zero to begin with and as the algorithm progresses τ is decreased by a factor of 0.99 at each iteration to make the prior term more and more comparable in magnitude to the noise term. As explained in section 3.3 this approach tends to avoid most local minima and converges at solutions that are nearly global.

Results

Fig 5.10 shows the simulated representation of a disk placed beneath the soil surface. The horizontal axis represents the line along which the GPR moves (assumed from left to right) and the vertical axis denotes the depth of the object. As most of the waves from the transmitter bounce off the top of the object, only the upper half of the disk is used in the simulation.



Fig 5.10 Simulated image of the upper half of a disk placed under a soil surface.

The result of the convolution from can be seen in Fig 5.11. The disk now looks like a hyperbola, which has its center coinciding with the center of the disk. As explained, this occurs due to the breadth of the signal spread of the GPR. The signals get attenuated as the distance traveled increases and hence pixels at a greater depth are relatively dimmer than the ones higher up.

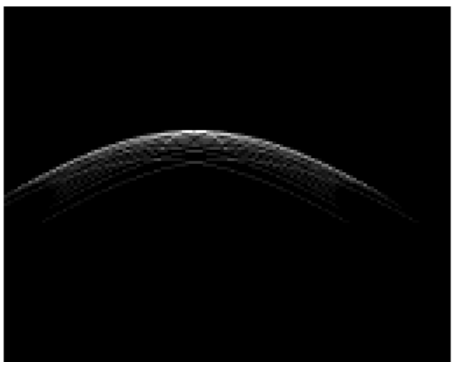

Figure 5.11. Hyperbolic Representation (convolution) of the disk caused by the signal of the GPR.

The MFA algorithm is applied to the image in Fig 5.11. After using the measured image (Fig 5.11) as the initial estimate for the MFA algorithm, the algorithm converges to the image in Fig 5.12.

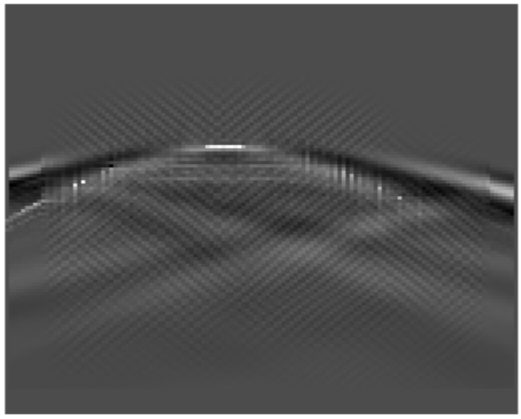

Figure 5.12. Reconstruction of the disk using the MFA algorithm.

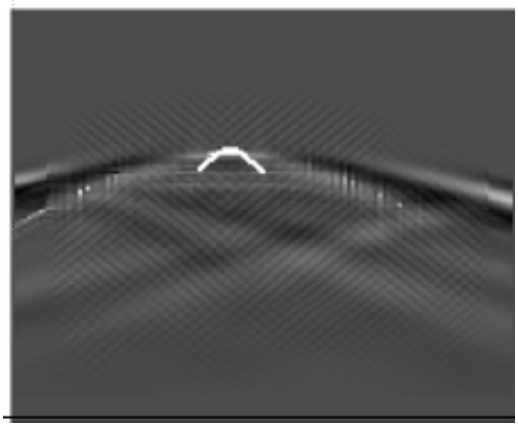

Figure 5.13. What the complete disk would have looked like

It can be seen that most only the area corresponding to the top of the disk is bright. Fig 5.13 illustrates what the complete reconstruction would have looked like. A possible explanation as to why only part of the disk is visible in Fig 5.12 is that only the top of the disk remains intact after the initial convolution (Fig 5.11). The hyperbolae resulting from the surface of the disk mixes up with the area corresponding to the remaining portions of the disk, which get obscured and appear as part of the spread caused by the surface pixels. The reconstruction is unable to differentiate between the original portion and the spread. This causes the algorithm to eliminate the original area along with most of the spread during the reconstruction. As a result only the original part of the disk that wasn't corrupted by the spread appears as a bright line in Fig 5.12.

The energy curve for successive iterations of the MFA algorithm is shown in Fig 5.14. The energy term indicates the difference in images in consecutive iterations, also considered as an error. The algorithm converges to a solution when this error is minimized. In the case above, this happens at the 92nd iteration after which the algorithm moves away from the solution.

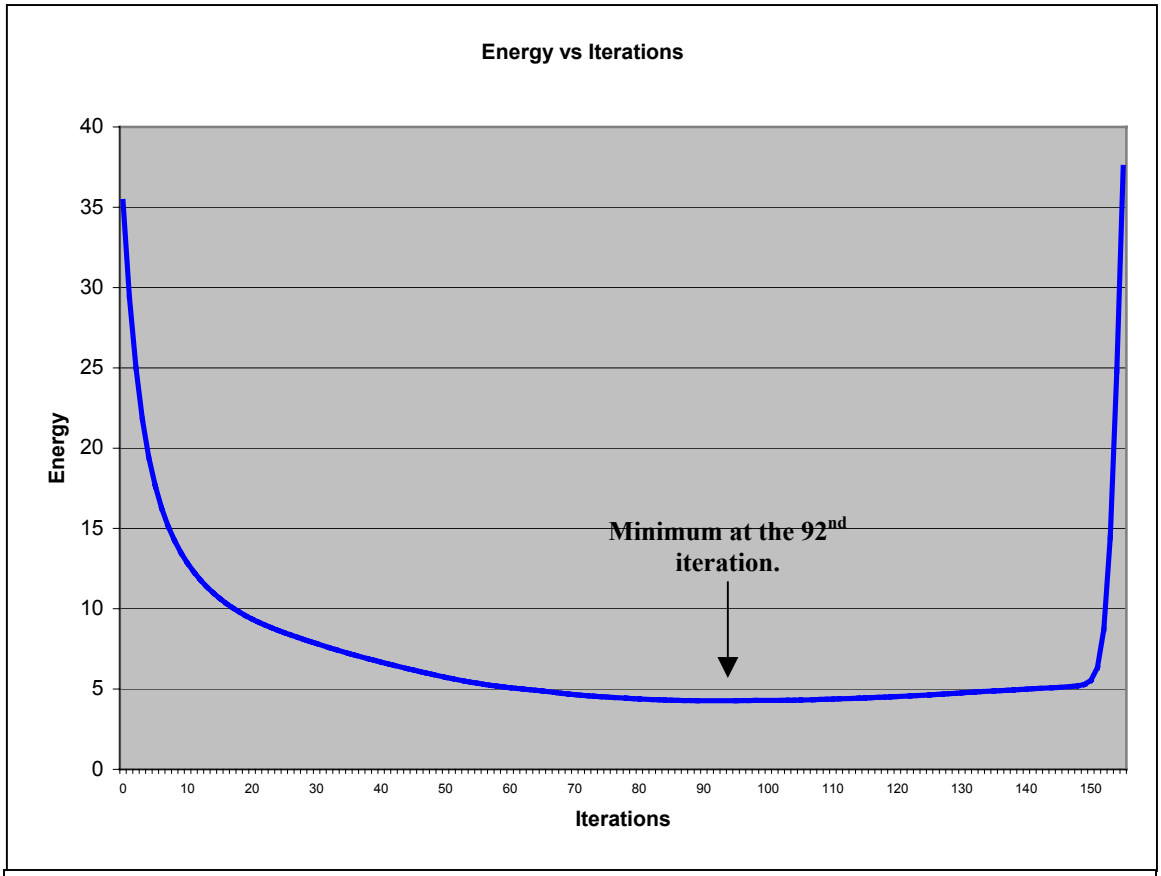

Figure 5.14. Energy Curve of the MFA algorithm.

Fig 5.15 shows the effect of noise on the reconstruction. The error is close to 0 when minimal noise is present and increases over to about 10 times that value when the SNR is 10. It then

increases steeply for lower SNR values. Error values greater than 75 units create a difficulty in object detection.

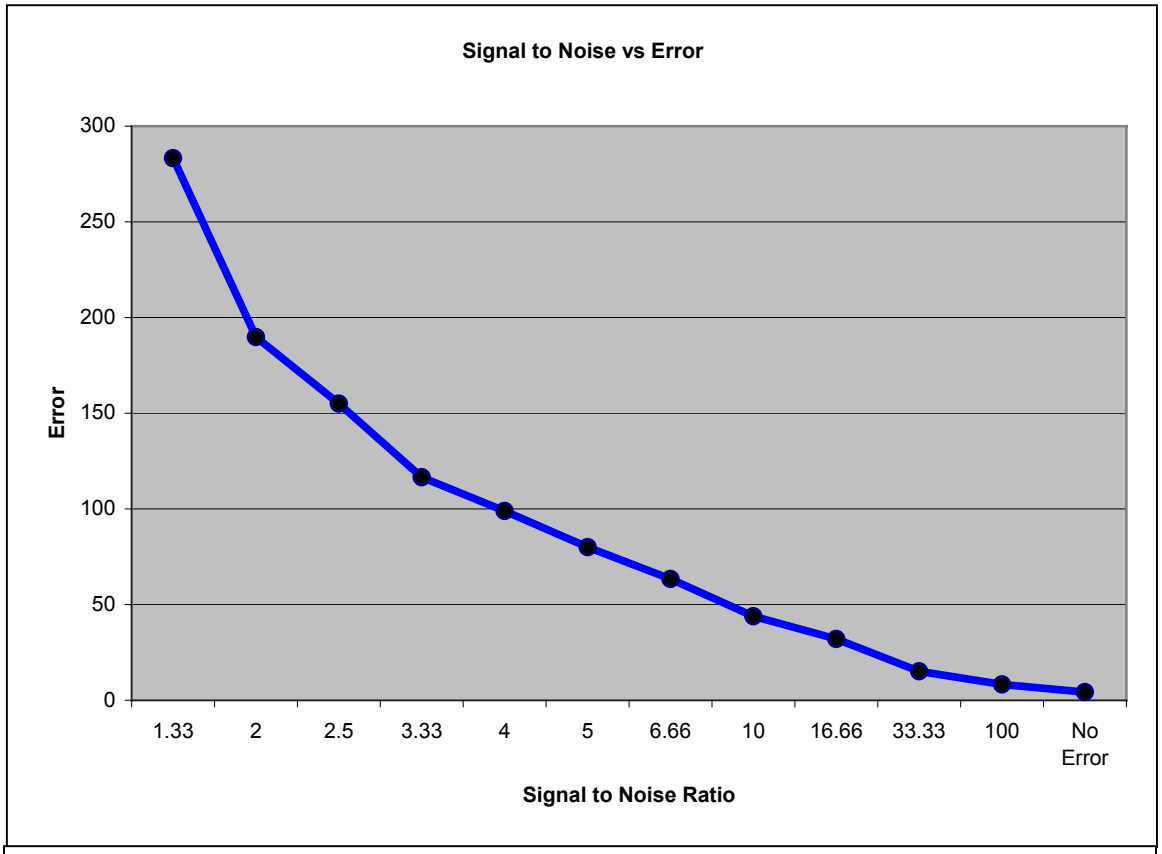

Fig 5.15 Graph of Signal to Noise Ratio vs Error.

6. CONCLUSION

The process of reconstruction of images from the GPR is broken down into various parts due to the complex nature of the data recording process of the RAMAC GPR. Many papers have presented techniques to reconstruct part of the data, but very few have addressed the reconstruction in its entirety.

Due to the proximity of the antenna to the receiver, the instrument records and superimposes the transmitted wave over the received signals. The process of utility detection is complicated due to the strength of the transmitted signal. We propose two methods to remove the transmitted signal. The "Subtract Transmitted Pulse" method subtracts a sample-transmitted pulse from the entire image. This algorithm runs fast but tends to leave behind heavy traces of the input signal. The "Subtract Mean Trace" method takes the average of all pixels within a horizontal window and subtracts this average from all the elements in that window. The running time of this algorithm is slower as compared to the previous technique but it removes the transmitted wave almost completely. The ideal window size was found to be between 30 and 40 pixels.

As a single pulse of the GPR is not an impulse but rather a wave that looks similar to a Gaussian Modulated Sine Wave (GMSW), the reflections from the utilities are magnitudes of this wave. Hence any object in the image appears as a collection of black and white bands. We used a technique based on the linear correlation coefficient (LCC) to reconstruct the pulses. However, we assume that there would not be a case where two objects would be present, one on top of the other. We can follow this assumption, as in that case most of the

incident wave would be reflected by the upper utility, leaving an extremely minute magnitude of the incident wave to be reflected by the lower utility, which might not be strong enough to show up in the image. The LCC technique works very well on simulated data when the GMSW was used. It works equally well on actual data from the GPR, but in this case the actual wave of the GPR is used as the incident wave.

The final part of the reconstruction is to invert the hyperbolae that are caused due to the signal spread of the GPR. To do this, we use a technique that is based on the optimization of an objective function. We construct the objective function, with a combination of data present in the measured image and the known characteristics of the actual undistorted signal. The optimization is done based on a technique called mean field annealing that uses gradient descent. Gradient descent is a minimization technique that computes the slope of a function and moves in the opposite direction in search of a minimum. Mean field annealing (which is a modification of simulated annealing) is an annealing algorithm that uses gradient descent and makes the search faster but avoids most local minima and provides solutions to optimization problems that are nearly global, Gradient descent is based on the assumption that the function that needs to be minimized is differentiable. The reconstruction works well for images that have only one hyperbola. The reconstruction of hyperbolae present in actual GPR data requires a marginally altered kernel in the objective function.

7. FUTURE WORK

In the reconstruction of the hyperbolae caused by the signal spread, the objective function uses a kernel models the signal spread. Although this kernel works well in the reconstruction of synthetic data, it needs to be modified in order to reconstruct actual data from the GPR. Current experiments show a minor difference between the structures of the hyperbolae that are created in the synthetic data and the ones present in actual data. When the modification in the kernel makes both the hyperbolic representations identical, the reconstruction will work equally well for real data.

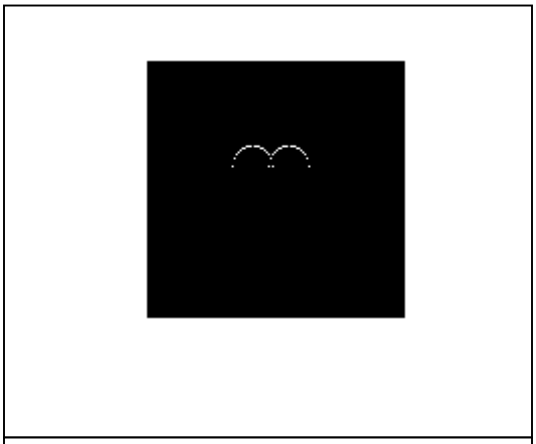

Fig 7.1 Two disks placed side by side.

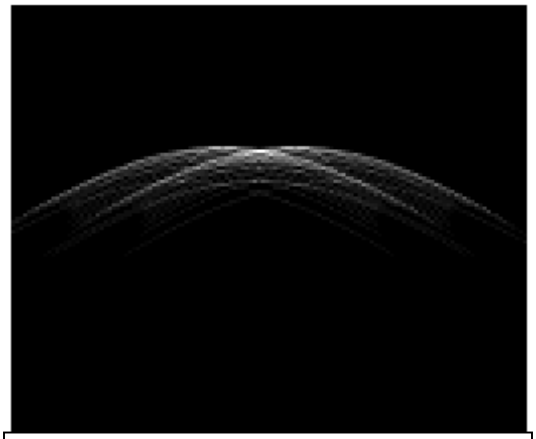

Fig 7.2 Hyperbolic representations of the two disks (Simulated).

The presence of two utilities beside each other (Fig 7.1) creates hyperbolic representations as shown in Fig 7.2. In this case the intersection of the two hyperbolae appears as a hyperbola itself.

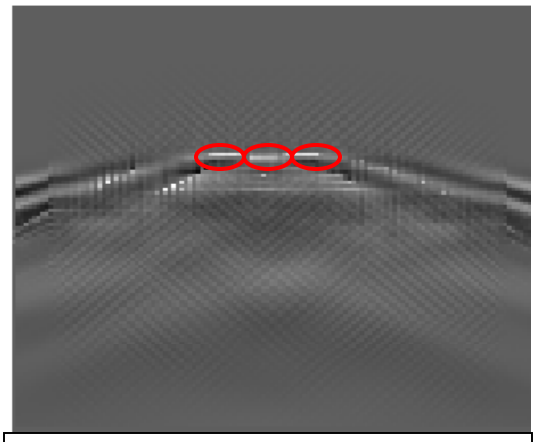

Fig 7.3 Resulting Reconstruction using the MFA algorithm.

Hence as a result (Fig 7.3) of the minimization three disks (three lines inside the red circles) are seen in the final image. Further research is required to isolate this condition and reconstruct only the original disks.

Further research is also required to combine the two reconstruction techniques into one so that only a single algorithm would relocate the utilities from a filtered image.

BIBLIOGRAPHY

1. Aaltonen J., Nissen J., (2002) "Geological mapping using GPR and differential GPS positioning: a case study", *Proceedings of the Ninth International Conference on GPR, Santa Barbara, California,* Stockholm AB (Sweden), 207-210.

2. Annan A. P., Cosway S. W., De Souza T., (2002) "Application of GPR to map concrete to delineate embedded structural elements and defects", *Proceedings of the Ninth International Conference on GPR, Santa Barbara, California,* Canada, 359-364.

3. Bilbro G., Snyder W. (1990), "Mean Field Annealing, an application to image noise removal," *Journal of Neural Network Computing*.

4. Cardimona S., Webb J., Lippincott T., (2000) *Ground Penetrating Radar*. Department of Geology and Geophysics, University of Missouri Rolla, Rolla, MO.

5. Chen C. C., Higgins M. B., (2002) "Evolution of buried UXO classification using broadband fully polarimetric GPR", *Proceedings of the Ninth International Conference on GPR, Santa Barbara, California,* 228-234.

6. Colombo S., Giannopoulos A., Forde M. C., (2002) "Depth of first detectable defect in a masonry wall using GPR", *Proceedings of the Ninth International Conference on GPR, Santa Barbara, California*, 371-375.

7. Daniels D. J, (1996) *Surface Penetrating Radar*, London: Institution of Electrical Engineers.

8. Daniels, J.J, (1985), "Borehole geophysical techniques for mineral exploration and evaluation" *AIME Transactions of Annual Meeting*, New York.

9. Daniels, J.J, and Dyck A.V., (1984) "Borehole resistivity and electromagnetic methods applied to mineral exploration" *IEEE Trans. on Geoscience and Remote Sensing*, vol. GE-22, no. 1, p. 80-87.

10. Derobert X., Abraham O., (2002) "Review of NDT methods on a weak post-tensioned beam before autopsy", *Proceedings of the Ninth International Conference on GPR, Santa Barbara, California*, 365-370.

11. Emilsson J., Englund P., (2002) "Simple Method for estimation of water content of roadbeds using multi-offset GPR", *Proceedings of the Ninth International Conference on GPR, Santa Barbara, California,* 422-426.

12. Evangelista R., Magee P., Wedepohl E., (2002) "3D Imaging of an Iron Age archaeological site: GPR analysis at Muweilah, U.A.E", *Proceedings of the Ninth International Conference on GPR, Santa Barbara, California*, 108-114.

13. Gader I. S., Mystkowski M., and Zhao Y., (2001) "Landmine Detection with Ground Penetrating Radar Using Hidden Markov Models," *IEEE Transactions on Geoscience and Remote Sensing*, Vol. 39, No. 6, pp. 1231–1244.

14. Gestel J., Stoffa P., (2000) "Migration using multi-configuration GPR data," *Proceedings of the Eight International Conference on GPR, Gold Coast Australia*, 448-452.

15. Giannopoulos A., Macintyre P., Rodgers S., Forde M. C., (2002) "GPR detection of voids in post-tensioned concrete bridge beams", *Proceedings of the Ninth International Conference on GPR, Santa Barbara, California,* 376-382.

16. Grasmueck M., Weger R., (2002) "Reassessment of local paleocurrent directions in the Miami oolitic limestone with 3D GPR", *Proceedings of the Ninth International Conference on GPR, Santa Barbara, California*, 211-216.

17. Heincke B., Spillmann T., Horstmeyer H., Green A. G., (2002) "3D georadar surveying in areas of moderate topographic relief", *Proceedings of the Ninth International Conference on GPR, Santa Barbara, California*, 223-227.

18. Herman H., (1997) "Robotic Subsurface Mapping using GPR data", *Technical Report CMU-RI-TR-97-19*, Carnegie Mellon University, Pittsburgh, Pennsylvania.

19. Hugenschmidt J., (2002) "One-to-One comparison between radar results and reality on a concrete bridge", *Proceedings of the Ninth International Conference on GPR, Santa Barbara, California*, 427-43

20. Jol H. M., DeChaine R. D., Eisenman R., (2002) "Archaeological GPR investigation at Rennes-le-Chateau, France", *Proceedings of the Ninth International Conference on GPR, Santa Barbara, California*, 91-95.

21. Liu L., Guo T., (2002) "Dielectric property of asphalt pavement specimens in dry, water-saturated, and frozen conditions", *Proceedings of the Ninth International Conference on GPR, Santa Barbara, California*, 410-415.

22. Martinez A., Byrnes A., (2001) "Modeling dielectric-constant values of geological materials – An aid to GPR data collection and interpretation", *Current Research in Earth Sciences*, Bulletin 247, part 1.

23. Millard S. G., Davis J., Huang Y., Bungey J. H., (2002) "Wideband system for measuring dielectric properties of concrete", *Proceedings of the Ninth International Conference on GPR, Santa Barbara, California*, 416-421.

24. Moorman B. J., Maillol J. M., Williams J. L., Walter F. S., Glanzman W. D., (2002) "Imaging the Past: archaeological radar stratigraphic analysis at Mahram Bilqis",

Proceedings of the Ninth International Conference on GPR, Santa Barbara, California, 96-101.

25. Moran M., Greenfield R., Arcone S., Delaney A. J., (2000) "Multidimensional GPR array processing using Kirchhoff migration", *Journal of Applied Geophysics*, v. 43, issue 2-4,p. 281-295.

26. Radzevicius S., (2001) "Dipole antenna properties and their effects on GPR data", *Technical Report*, Ohio State University.

27. Roth F., Genderen P., Verhaegen M., (2002) "Radar response approximations for buried plastic landmines", *Proceedings of the Ninth International Conference on GPR, Santa Barbara, California*, 234-240.

28. Snyder G.L., Patten L.L., and Daniels J.J., (1987), "Mineral resources of the Mount Zirkel Wilderness and Northern Park Range Vicinity, Jackson and Rautt Counties, Colorado": *U.S. Geol. Survey Bull* 1554 Washington D. C.

29. Snyder W., Bilbro G., Mann R. (1991), "Mean Field approximation minimizes relative entropy", *Journal of the Optical Society of America A,* 8(2).

30. Snyder W., Hsiao M. L., Campbell J. N., (1993) "Restoration of ultrasonic NDE images," in *IEEE Transactions on Industrial Electronics*, Vol. 40, No. 2,

31. Snyder W., Han Y., Bilbro G., Whitaker R., Pizer S., (1995) "Image Relaxation: Restoration and Feature Extraction," *IEEE Transactions on Pattern Analysis and Machine Intelligence.*

32. Teixeira F. L., Chew W. C., Straka M., Oristaglio M. L., and Wang T. (1998) "Finite-Difference Time-Domain Simulation of Ground Penetrating Radar on Dispersive,

Inhomogeneous and Conductive Soils" *IEEE Transactions on Geoscience and Remote Sensing*,

33. Utsi E., Alani A., (2002) "Barcombe Roman Villa: an exercise in GPR time slicing and comparative geophysics", *Proceedings of the Ninth International Conference on GPR, Santa Barbara, California*, 102-107.

34. Van der Lijn F. (2002) "Deconvolution of the impulse response of mine like targets using GPR signals", *Technical Report*, University of Twente.

35. Yarovoy A. G., Ligthart L. P., Shukin A. D. (2002) "Full-polarimetric video impulse radar for landmine detection", *Proceedings of the Ninth International Conference on GPR, Santa Barbara, California*, 246-251.

36. Zanzi L., Lauldi M., (2002) "Ultrahigh-frequency radar sensor for humanitarian demining tested on different scenarios in 3D imaging mode", *Proceedings of the Ninth International Conference on GPR, Santa Barbara, California*, 240-246.